

1 **Tropopause Evolution in a Rapidly Intensifying Tropical Cyclone: A Static**  
2 **Stability Budget Analysis in an Idealized, Axisymmetric Framework**

3 Patrick Duran\* and John Molinari

4 *University at Albany, State University of New York, Albany, NY*

5 \**Corresponding author address:* Department of Atmospheric and Environmental Sciences, Univer-  
6 sity at Albany, State University of New York, 1400 Washington Avenue, Albany, NY.

7 E-mail: pduran2008@gmail.com

## ABSTRACT

8 Large changes in tropopause-layer static stability are observed during the  
9 rapid intensification (RI) of an idealized, axisymmetric tropical cyclone (TC).  
10 Over the eye, static stability near the tropopause decreases and the cold-point  
11 tropopause height rises by up to 4 km at the storm center. Outside of the eye,  
12 static stability increases considerably just above the cold-point tropopause,  
13 and the tropopause remains near its initial level.

14 A budget analysis reveals that advection contributes to the static stability  
15 tendencies at all times throughout the upper troposphere and lower strato-  
16 sphere. Differential advection is particularly important within the eye, where  
17 it acts to destabilize the layer near and above the cold-point tropopause.  
18 Outside of the eye, a radial-vertical circulation develops during RI, with  
19 strong outflow below the tropopause and weak inflow above. Vertical wind  
20 shear above and below the upper-tropospheric outflow maximum induces tur-  
21 bulence, which provides forcing for both destabilization and stabilization  
22 in the tropopause layer. Meanwhile, as organized convection reaches the  
23 tropopause, radiative heating tendencies at the top of the cirrus canopy gen-  
24 erally act to destabilize the upper troposphere and stabilize the lower strato-  
25 sphere. Turbulent mixing and radiative heating combine to play an important  
26 role in the development of the strong stable layer immediately above the cold-  
27 point tropopause during RI. The results suggest that turbulence and radiation,  
28 alongside advection, play fundamental roles in the upper-level static stability  
29 evolution of TCs.

## 30 **1. Introduction**

31 After undergoing a remarkably rapid intensification (RI), Hurricane Patricia (2015) set a new  
32 record as the strongest tropical cyclone (TC) ever observed in the Western Hemisphere (Kim-  
33 berlain et al. 2016; Rogers et al. 2017). High-altitude dropsonde observations taken during the  
34 Tropical Cyclone Intensity (TCI) experiment captured this RI in unprecedented detail (Doyle et al.  
35 2017). These observations revealed dramatic changes in the structure of the cold-point tropopause  
36 and upper-level static stability as the storm intensified (Duran and Molinari 2018).

37 When Patricia was at tropical storm intensity, shortly before RI commenced, a strong inversion  
38 layer existed just above the cold-point tropopause. During the first half of the RI period, this  
39 inversion layer weakened throughout Patricia’s inner core, with the weakening most pronounced  
40 over the developing eye. By the time the storm reached its maximum intensity of  $95 \text{ m s}^{-1}$ , the  
41 inversion layer over the eye had disappeared almost completely, which was accompanied by a  
42 greater than 1-km increase in the tropopause height. Meanwhile over the eyewall region, the static  
43 stability increased and the tropopause remained near its initial level. The mechanisms that might  
44 have led to this tropopause-layer variability will be investigated in the current paper using idealized  
45 simulations.

46 Despite the importance of tropopause-layer thermodynamics in theoretical models of hurri-  
47 canes (Emanuel and Rotunno 2011; Emanuel 2012), most observational studies of the upper-  
48 tropospheric structure of TCs are decades old. Recently, however, Komaromi and Doyle (2017)  
49 found that stronger TCs tended to have a higher and warmer tropopause over their inner core than  
50 weaker TCs. Their results are consistent with the evolution observed over the inner core of Hur-  
51 ricane Patricia, in which the tropopause height increased and the tropopause temperature warmed  
52 throughout RI (Duran and Molinari 2018).

53 Idealized simulations of a TC analyzed by Ohno and Satoh (2015) suggested that the develop-  
54 ment of an upper-level warm core near the 13-km level acted to decrease the static stability near the  
55 tropopause within the eye (compare their Figs. 9,10). Although the mechanisms that might drive  
56 this static stability evolution have not been examined explicitly, Stern and Zhang (2013) described  
57 the development of the TC warm core using a potential temperature ( $\theta$ ) budget analysis. They  
58 found that radial and vertical advection both played important roles in warm core development  
59 throughout RI, and subgrid-scale diffusion became particularly important during the later stage of  
60 RI. To our knowledge, the only paper that has examined explicitly the static stability evolution in  
61 a modeled TC is Kepert et al. (2016), but their analysis was limited to the boundary layer. The  
62 analysis herein is based upon that of Stern and Zhang (2013), except using a static stability budget  
63 similar to that of Kepert et al. (2016), with a focus on the upper troposphere and lower stratosphere.

## 64 **2. Model Setup**

65 The numerical simulations were performed using version 19.4 of Cloud Model 1 (CM1) de-  
66 scribed in Bryan and Rotunno (2009). The equations of motion were integrated on a 3000-km-  
67 wide, 30-km-deep axisymmetric grid with 1-km horizontal and 250-m vertical grid spacing. The  
68 computations were performed on an  $f$ -plane at 15°N latitude, over a sea surface with constant  
69 temperature of 30.5°C, which matches that observed near Hurricane Patricia (2015; Kimberlain  
70 et al. 2016). Horizontal turbulence was parameterized using the Smagorinsky scheme described  
71 in Bryan and Rotunno (2009, pg. 1773), with a prescribed mixing length that varied linearly from  
72 100 m at a surface pressure of 1015 hPa to 1000 m at a surface pressure of 900 hPa. Vertical  
73 turbulence was parameterized using the formulation of Markowski and Bryan (2016, their Eq. 6),  
74 using an asymptotic vertical mixing length of 100 m. A Rayleigh damping layer was applied out-  
75 side of the 2900-km radius and above the 25-km level to prevent spurious gravity wave reflection

at the model boundaries. Microphysical processes were parameterized using the Thompson et al. (2004) scheme and radiative heating tendencies were computed every two minutes using the Rapid Radiative Transfer Model for GCMs (RRTMG) longwave and shortwave schemes (Iacono et al. 2008). The initial temperature and humidity field was horizontally homogeneous and determined by averaging all Climate Forecast System Reanalysis (CFSR) grid points within 100 km of Patricia's center of circulation at 18 UTC 21 October 2015. The vortex described in Rotunno and Emanuel (1987, their Eq. 37) was used to initialize the wind field, setting all parameters equal to the values used therein.

Although hurricanes simulated in an axisymmetric framework tend to be more intense than those observed in nature, the intensity evolution of this simulation matches reasonably well with that observed in Hurricane Patricia. After an initial spin-up period of about 20 hours, the modeled storm (Fig. 1, blue lines) began an RI period that lasted approximately 30 hours. After this RI, the storm continued to intensify more slowly until the maximum 10-m wind speed reached  $89 \text{ m s}^{-1}$  and the sea-level pressure reached its minimum of 846 hPa, 81 hours into the simulation. Hurricane Patricia (red stars) exhibited a similar intensity evolution prior to its landfall, with an RI period leading to a maximum 10-m wind speed of  $95 \text{ m s}^{-1}$  and a minimum sea-level pressure of 872 hPa.

### 3. Budget Computation

The static stability can be expressed as the squared Brunt-Väisälä frequency:

$$N_m^2 = \frac{g}{T} \left( \frac{\partial T}{\partial z} + \Gamma_m \right) \left( 1 + \frac{T}{R_d/R_v + q_s} \frac{\partial q_s}{\partial T} \right) - \frac{g}{1 + q_t} \frac{\partial q_t}{\partial z}, \quad (1)$$

where  $g$  is gravitational acceleration,  $T$  is temperature,  $R_d$  and  $R_v$  are the gas constants of dry air and water vapor, respectively,  $q_s$  is the saturation mixing ratio,  $q_t$  is the total condensate mixing

ratio, and  $\Gamma_m$  is the moist-adiabatic lapse rate:

$$\Gamma_m = g(1 + q_t) \left( \frac{1 + L_v q_s / R_d T}{c_{pm} + L_v \partial q_s / \partial T} \right), \quad (2)$$

where  $L_v$  is the latent heat of vaporization and  $c_{pm}$  is the specific heat of moist air at constant pressure. In the tropopause layer,  $q_s$ ,  $\partial q_s / \partial T$ , and  $\partial q_t / \partial z$  approach zero. In this limiting case, Eq. 1 reduces to:

$$N^2 = \frac{g}{\theta} \frac{\partial \theta}{\partial z}, \quad (3)$$

where  $\theta$  is the potential temperature.

To compute  $N^2$ , CM1 uses Eq. 1 in saturated environments and Eq. 3 in sub-saturated environments. For simplicity, however, only Eq. 3 will be employed for the budget computations<sup>1</sup>.

Taking the time derivative of Eq. 3 yields the static stability tendency:

$$\frac{\partial N^2}{\partial t} = \frac{g}{\theta} \frac{\partial}{\partial z} \frac{\partial \theta}{\partial t} - \frac{g}{\theta^2} \frac{\partial \theta}{\partial z} \frac{\partial \theta}{\partial t}, \quad (4)$$

where the potential temperature tendency,  $\partial \theta / \partial t$ , can be written, following Bryan (cited 2018):

$$\frac{\partial \theta}{\partial t} = -u \frac{\partial \theta}{\partial r} - w \frac{\partial \theta}{\partial z} + HTURB + VTURB + MP + RAD + DISS \quad (5)$$

Each term on the right-hand side of Eq. 5 represents a  $\theta$  budget variable, each of which is output directly by the model every minute. Since the first term on the right-hand side of Eq. 4 is larger than the second term throughout most of the tropopause layer (not shown), the contribution of each of the terms in Eq. 5 to the  $N^2$  tendency can be interpreted in light of a vertical gradient of each term.

Taking the vertical gradient of the first two terms on the right-hand side of Eq. 5 yields the time tendency of the vertical  $\theta$  gradient due to horizontal and vertical advection<sup>2</sup>:

---

<sup>1</sup>The validity of this approximation will be substantiated later in this section.

<sup>2</sup>These terms include the tendencies due to implicit diffusion in the fifth-order finite differencing scheme, which are separated from the advection

$$\left( \frac{\partial}{\partial t} \frac{\partial \theta}{\partial z} \right)_{adv} = -u \frac{\partial}{\partial r} \frac{\partial \theta}{\partial z} - w \frac{\partial}{\partial z} \frac{\partial \theta}{\partial z} - \frac{\partial u}{\partial z} \frac{\partial \theta}{\partial r} - \frac{\partial w}{\partial z} \frac{\partial \theta}{\partial z}. \quad (6)$$

113 The first two terms on the right-hand side of Eq. 6 represent advection of static stability by the  
 114 radial and vertical wind, respectively. These terms act to rearrange the static stability field, but  
 115 cannot strengthen or weaken static stability maxima or minima. The third and fourth terms on the  
 116 right-hand side of Eq. 6 represent, respectively, the tilting of isentropes in the presence of vertical  
 117 wind shear, and the stretching or squashing of isentropes by vertical gradients of vertical velocity.  
 118 Since these terms involve velocity gradients, they can act to strengthen or weaken static stability  
 119 maxima or minima through differential advection. For example, since the  $\theta$  of the air flowing  
 120 out of the eyewall into the upper-tropospheric outflow layer increases as the TC intensifies,  $\theta$  in-  
 121 creases locally within the outflow layer. This acts to increase  $\partial \theta / \partial z$  below the outflow maximum  
 122 and decrease  $\partial \theta / \partial z$  above, thereby modifying the static stability field. Similarly, the decay of  
 123 updrafts with height at the top of convective towers can act to increase  $\partial \theta / \partial z$  through squashing  
 124 of isentropes.

125 Returning to Eq. 5, HTURB and VTURB are the  $\theta$  tendencies from the horizontal and vertical  
 126 turbulence parameterizations, MP is the tendency from the microphysics scheme, RAD is the  
 127 tendency from the radiation scheme, and DISS is the tendency due to turbulent dissipation. This  
 128 equation neglects Rayleigh damping, since the entire analysis domain lies outside of the regions  
 129 where damping is applied. Each term in Eq. 5 is substituted for  $\partial \theta / \partial t$  in Eq. 4, yielding the  
 130 contribution of each budget term to the static stability tendency. These terms are summed, yielding  
 131 an instantaneous "budget change" in  $N^2$  every minute. The budget changes are then averaged over  
 132 24-hour periods and compared to the total model change in  $N^2$  over that same time period, i.e.:

$$\Delta N_{budget}^2 = \frac{1}{\delta t} \sum_{t=t_0}^{t_0+\delta t} \frac{\partial N^2}{\partial t} \Big|_t \quad (7)$$

$$\Delta N_{model}^2 = N_{t_0+\delta t}^2 - N_{t_0}^2 \quad (8)$$

$$Residual = \Delta N_{model}^2 - \Delta N_{budget}^2 \quad (9)$$

where  $t_0$  is an initial time and  $\delta t$  is 24 hours.

Eqs. 7-9 are plotted for three consecutive 24-hour periods in Fig. 2. For this and all subsequent radial-vertical cross sections, a 1-2-1 smoother is applied once in the radial direction to eliminate  $2\Delta r$  noise that appears in some of the raw model output and calculated fields. The left column of Fig. 2 depicts the model changes computed using Eq. 8, together with Eq. 1 in saturated environments and Eq. 3 in subsaturated environments. The center column depicts the budget changes computed using Eq. 7 together with Eq. 3 throughout the entire domain. Thus, the left column includes the effect of moisture in the  $N^2$  computations, whereas the center column neglects moisture. The right column depicts the residuals, computed using Eq. 9 (i.e. the left column minus the center column.) In every 24-hour period, the budget changes are nearly identical to the model changes, which is reflected in the near-zero residuals in the right column. This indicates that the budget accurately represents the model variability, which implies that the neglect of moisture in the budget computation introduces negligible error within the analysis domain<sup>3</sup>.

In the tropopause layer, some of the budget terms are small enough to be ignored. To determine which of the budget terms are most important, a time series of the contribution of each of the budget terms in Eq. 5 to the tropopause-layer static stability tendency is plotted in Fig. 3. For this figure, each of the budget terms is computed using the method described in Section 3, except with 1-hour averaging intervals instead of 24-hour intervals. The absolute values of these tendencies are then averaged over the radius-height domain of the plots shown in Fig. 2 and plotted as a time

---

<sup>3</sup>This is not the case in the lower- and mid-troposphere, where the residual actually exceeds the budget tendencies in many places, likely due to the neglect of moisture; thus we limit this analysis to the upper troposphere and lower stratosphere.



154 series<sup>4</sup>. Advection (Fig. 3, red line) plays an important role in the mean tropopause-layer static  
155 stability tendency at all times, and vertical turbulence (Fig. 3, blue line) and radiation (Fig. 3, dark  
156 green line) also contribute significantly. The remaining three processes - horizontal turbulence,  
157 microphysics, and dissipative heating - are negligible everywhere outside of the eyewall, and do  
158 not play important roles in the mesoscale tropopause variability.

159 The preceding analysis indicates that, at all times, three budget terms dominate the tropopause-  
160 layer static stability tendency: advection, vertical turbulence, and radiation. Variations in the  
161 magnitude and spatial structure of these terms drive the static stability changes depicted in Fig. 2;  
162 subsequent sections will focus on these variations and what causes them.

## 163 4. Results

### 164 a. Static stability evolution

165 The average  $N^2$  over the first day of the simulation (Fig. 4a) indicates the presence of a weak  
166  $N^2$  maximum just above the cold-point tropopause. Over the subsequent 24 hours, during the  
167 RI period, the  $N^2$  within and above this layer decreased within the 25-km radius (Fig. 4b). This  
168 decreasing  $N^2$  corresponded to an increase in the tropopause height within the developing eye,  
169 maximized at the storm center. Outside of the eye, meanwhile, the tropopause height decreased  
170 over the eyewall region (25-60-km radius) and increased only slightly outside of the 60-km ra-  
171 dius. In this outer region, the  $N^2$  maximum just above the tropopause strengthened during RI.  
172 These trends continued as the storm's intensity leveled off in the 48-72-hour period (Fig. 4c). The  
173 tropopause height increased to nearly 21 km at the storm center and sloped sharply downward to

---

<sup>4</sup>It will be seen in subsequent figures that each of the terms contributes both positively and negatively to the  $N^2$  tendency within the analysis domain. Thus, taking an average over the domain tends to wash out the positive and negative contributions. To circumvent this problem, the absolute value of each of the terms is averaged.

174 16.3 km on the inner edge of the eyewall, near the 30 km radius. Static stability outside of the eye,  
175 meanwhile, continued to increase just above the cold-point tropopause. This  $N^2$  evolution closely  
176 follows that observed in Hurricane Patricia (2015; Duran and Molinari 2018). The mechanisms  
177 that led to these  $N^2$  changes will be investigated in the subsequent sections.

## 178 *b. Static stability budget analysis*

179 *(i) 0-24 hours* The weakening of the lower-stratospheric  $N^2$  maximum during the initial spin-up  
180 period is reflected in the total  $N^2$  budget change over this time (Fig. 5a). The layer just above  
181 the cold-point tropopause was characterized by decreasing  $N^2$  (purple shading), maximizing at the  
182 storm center. At and immediately below the tropopause, meanwhile, saw increasing  $N^2$  during this  
183 time period. Although these tendencies extended out to the 200-km radius, they were particularly  
184 pronounced at innermost radii. A comparison of the contributions of advection (Fig. 5b), vertical  
185 turbulence (Fig. 5c), and radiation (Fig. 5d) reveals that advection was the primary driver of the  
186  $N^2$  tendency during this period, acting to stabilize near and just below the tropopause and destabi-  
187 lize above. Although vertical turbulence acted in opposition to advection (i.e. it acted to stabilize  
188 regions that advection acted to destabilize), the magnitude of the advective tendencies was larger,  
189 particularly at the innermost radii. The sum of advection and vertical turbulence (Fig. 5e) almost  
190 exactly replicated the static stability tendencies above the tropopause. Radiative tendencies, mean-  
191 while, (Fig. 5d) acted to destabilize the layer below about 16 km and stabilize the layer between  
192 16 and 17 km. The sum of advection, vertical turbulence, and radiation (Fig. 5f) reproduces the  
193 total change in  $N^2$  almost exactly.

194 *(ii) 24-48 hours* During the RI period,  $N^2$  within the eye generally decreased above 16 km and  
195 increased below (Fig. 6a), with the destabilization above 16 km maximizing near the level of the  
196 mean cold-point tropopause. These tendencies at the innermost radii were driven almost entirely

197 by advection (Fig. 6b); vertical turbulence (Fig. 6c) and radiation (Fig. 6d) contributed negligibly  
198 to the static stability tendencies in this region.

199 Outside of the eye, the  $N^2$  evolution exhibited alternating layers of positive and negative tenden-  
200 cies. Near and above 18 km existed an upward-sloping region of decreasing  $N^2$  that extended out  
201 to the 180-km radius. In this region, neither vertical turbulence nor radiation exhibited negative  $N^2$   
202 tendencies; advection was the only forcing for this destabilization. Immediately below this layer,  
203 just above the cold-point tropopause, was a region of increasing  $N^2$  that sloped upward from 17 km  
204 near the 30-km radius to just below 18 km outside of the 100-km radius. Advection and vertical  
205 turbulence both contributed to this positive  $N^2$  tendency, with advection playing an important role  
206 below about 17.5 km and and turbulence playing an important role above. The sum of advection  
207 and turbulence (Fig. 6e) reveals two discontinuous regions of increasing  $N^2$  in the 17-18-km layer  
208 rather than one contiguous region. The addition of radiation to these two terms, however, (Fig. 6f)  
209 provides the link between these two regions, indicating that radiation also plays a role in strength-  
210 ening the stable layer just above the tropopause. In the 16-17-km layer, just below the cold-point  
211 tropopause, a horizontally-extensive layer of destabilization also was forced by a combination of  
212 advection, vertical turbulence, and radiation. The sum of advection and vertical turbulence ac-  
213 counts for only a portion of the decreasing  $N^2$  in this layer, and actually indicates forcing for  
214 stabilization near the 50-km radius and outside of the 130-km radius. Radiative tendencies over-  
215 come this forcing for stabilization in both of these regions to produce the radially-extensive region  
216 of destabilization observed just below the tropopause.

217 The sum of advection, vertical turbulence, and radiation (Fig. 6f) once again closely follows  
218 the observed  $N^2$  variability, except in the eyewall region, where the neglect of latent heating and  
219 horizontal turbulence introduces some differences.

220 (iii) 48-72 hours After the storm's maximum wind speed leveled off near  $80 \text{ m s}^{-1}$ , the magnitude  
221 of the static stability tendencies within the eye decreased to near zero (Fig. 7a).

222 Outside of the eye, however,  $N^2$  continued to decrease in the layer immediately surrounding the  
223 tropopause. The sum of advection and vertical turbulence (Fig. 7e) indicates that the increase of  
224  $N^2$  observed in the 17-18-km layer and inside of the 80-km radius cannot be attributed to these  
225 processes, since the sum of these two terms provided forcing for destabilization. Instead, radiation  
226 (Fig. 7d) provided the forcing for stabilization in this region. Outside of the 80-km radius, both  
227 advection (Fig. 7b) and vertical turbulence (Fig. 7c) provided forcing for stabilization near and  
228 just above the 18-km level. The sum of the two terms (Fig. 7e) indicates increasing  $N^2$  near the  
229 18-km level everywhere outside of the 80-km radius, but this stabilization is slightly weaker in  
230 the 90-120-km radial band than the observed value. The addition of radiation (Fig. 7f) provided  
231 the extra forcing for stabilization required to account for the observed increase in  $N^2$ . Outside  
232 of the 120-km radius, the region of radiative forcing for stabilization sloped downward, and the  
233 increase in  $N^2$  observed near 18 km can be explained entirely by a combination of advection and  
234 vertical turbulence. The layer of decreasing  $N^2$  observed near the tropopause was forced primarily  
235 by vertical turbulence and radiation. Within most of this region, advection provided strong forcing  
236 for stabilization, but this forcing was outweighed by the negative  $N^2$  tendencies induced by a  
237 combination of vertical turbulence and radiation.

## 238 5. Discussion

### 239 a. The role of advection

240 Advection played an important role in the tropopause-layer  $N^2$  evolution at all stages of intensi-  
241 fication, but for brevity, this section will focus only on the RI (24-48-hour) period. To investigate

the advective processes more closely, the individual contributions of horizontal and vertical advection during the RI period are shown in Fig. 8, along with the corresponding time-mean radial and vertical velocities and  $\theta$ . The  $N^2$  tendencies due to the two advective components (Fig. 8a,b) exhibited strong cancellation, consistent with flow that was nearly isentropic. There were, however, many regions in which flow crossed  $\theta$  surfaces; this flow accounted for all non-zero  $N^2$  tendencies due to advection previously seen in Fig. 6b.

During the RI period, strong radial and vertical circulations developed near the tropopause (Fig. 8c,d), which forced high-magnitude  $N^2$  tendencies due to advection (Fig. 8a,b). A layer of strong outflow formed at and below the tropopause during this period, with the outflow maximum (dashed cyan line) curving from the 14-km level at the 50-km radius to just below the 16-km level outside of the 80-km radius (Fig. 8c). Notably, the  $N^2$  tendency due to horizontal advection (Fig. 8a) tended to switch signs at this line, with stabilization below the outflow maximum and destabilization above. This is consistent with the outflow layer carrying air with increasingly large  $\theta$  from the eyewall to large radii as the storm intensified. This increase in  $\theta$  maximized near the outflow maximum, which acted to decrease  $\partial\theta/\partial z$  above the outflow maximum and increase it below. This mechanism is the same as that discussed in Trier and Sharman (2009), in which vertical wind shear in the outflow layer of a mesoscale convective system acted to modify the upper-tropospheric static stability through differential advection of isentropes.

Meanwhile in the lower stratosphere, a thin layer of 2-4 m s<sup>-1</sup> inflow developed a few hundred meters above the tropopause, similar to that which was observed in Hurricane Patricia (2015; Duran and Molinari 2018) and in previous modeling studies (e.g. Ohno and Satoh 2015; Kieu et al. 2016). Since the isentropes in this layer sloped slightly upward with radius (i.e.  $\partial\theta/\partial r < 0$ ), this inflow acted to import lower  $\theta$  air from outer radii to inner radii. Since the negative  $\theta$  tendencies

265 maximized at the level of maximum inflow, the layer below the inflow maximum destabilized and  
266 the layer above stabilized (Fig. 8a).

267 Curiously, horizontal advection contributed to the  $N^2$  tendency everywhere within the eye,  
268 even though the mean radial velocity there was near zero. Close examination of the model out-  
269 put revealed that these tendencies were forced by advective processes associated with inward-  
270 propagating waves. Although the radial velocity perturbations induced by these waves averaged  
271 out to zero, the advective tendencies forced by the radial velocity perturbations did not. Addition-  
272 ally, when these waves reached  $r=0$ , a dipole of vertical velocity resulted, with ascent above and  
273 descent below. For reasons that remain unclear, the regions of ascent were more persistent than the  
274 regions of descent, which resulted in the mean ascent observed near  $r=0$  above 17 km in Fig. 8b.

275 Vertical advection also played an important role in the tropopause-layer static stability evolution.  
276 Within the eye, subsidence dominated below 17 km, while mean ascent existed near the storm  
277 center above 17 km. Although the magnitude of the subsidence was larger at lower altitudes,  
278  $\partial\theta/\partial z$  was smaller there. Because  $\partial\theta/\partial z$  was smaller, the subsidence at lower levels could not  
279 accomplish as much warming as the subsidence at higher levels in the eye, consistent with the  
280 results of Stern and Zhang (2013). As a result, vertical advection within the eye acted to stabilize  
281 the layer below 16 km during RI.

282 Outside of the 27-km radius, ascent dominated the troposphere, while a 1.5-km-deep layer of  
283 descent existed immediately above the tropopause. These regions of ascent and descent converged  
284 just above the tropopause; this convergence acted to compact the isentropes in this layer and in-  
285 crease the static stability. Above the lower-stratospheric subsidence maximum, meanwhile, verti-  
286 cal advection acted to decrease  $N^2$ . Below the tropopause, differential vertical advection increased  
287  $N^2$  within the eyewall region and also at larger radii above the vertical velocity maximum at larger

radii. Outside of the eyewall and below the vertical velocity maximum, meanwhile, differential vertical advection acted to decrease  $N^2$ .

Comparing the  $N^2$  tendencies forced by horizontal (Fig. 8a) and vertical (Fig. 8b) advection to the total advective tendency seen in Fig. 6b reveals that horizontal advective tendencies dominated the troposphere, while vertical advective tendencies dominated the layer near and above the tropopause. Thus, tilting of isentropes in the vicinity of the upper-tropospheric outflow maximum appears to be the most important process governing the  $N^2$  tendency in the troposphere, whereas convergence of vertical velocity appears to be the most important process near the tropopause.

#### *b. The role of radiation*

During the initial spin-up period (0-24 hours; Fig. 9a), convection was not deep enough to deposit large quantities of ice near the tropopause and create a persistent cirrus canopy. Due to the lack of ice particles, the radiative heating tendencies during this period (Fig. 9b) were relatively small and confined to the region above a few particularly strong, although transient, convective towers. During RI (24-48 hours), the eyewall updraft strengthened and a radially-extensive cirrus canopy developed near the tropopause (Fig. 9c). The enhanced vertical gradient of ice mixing ratio at the top of the cirrus canopy induced strong diurnal-mean radiative cooling near the tropopause (Fig. 9d). This cooling exceeded  $0.6 \text{ K h}^{-1}$  in some places and sloped downward from the lower stratosphere into the upper troposphere, following the top of the cirrus canopy. A small radiative warming maximum also appeared outside of the 140-km radius below this region of cooling. These results broadly agree with those of Bu et al. (2014; see their Fig. 11a), whose CM1 simulations produced a  $0.3 \text{ K h}^{-1}$  diurnally-averaged radiative cooling at the top of the cirrus canopy and radiative warming within the cloud that maximized near the 200-km radius. This broad region of radiative cooling acted to destabilize the layer below the cooling maximum and stabilize the

311 layer above, which can be seen in Fig. 6d. The small area of net radiative heating outside of the  
312 140-km radius enhanced the destabilization above 16 km in this region and produced a thin layer  
313 of stabilization in the 15-16-km layer.

314 After the TC's RI period completed (48-72 hours), strong radiative cooling remained near the  
315 tropopause at inner radii (Fig. 9f), sloping downward with the top of the cirrus canopy to below  
316 the tropopause at outer radii. Cooling rates exceeded  $1 \text{ K h}^{-1}$  just above the tropopause between  
317 the 30- and 70-km radii. This value is more than three times the maximum cooling rate of  $0.3 \text{ K h}^{-1}$   
318 observed by Bu et al. (2014), a discrepancy that is a consequence of their larger vertical grid  
319 spacing compared to that used here, along with a contribution from differing radiation schemes. To  
320 compare our results to those of Bu et al. (2014), we ran a simulation identical to that described in  
321 Section 2, except using the NASA-Goddard radiation scheme and 625-m vertical grid spacing, to  
322 match those of Bu et al. (2014). This simulation produced a maximum 24-hour-average radiative  
323 cooling rate of  $0.3 \text{ K h}^{-1}$ , which agrees with that shown in Bu et al. (2014). Another simulation  
324 using 625-m vertical grid spacing and RRTMG radiation produced 24-hour-average cooling rates  
325 of up to  $0.6 \text{ K h}^{-1}$ , which is consistent with the WRF simulations of Bu et al. (2014). This suggests  
326 that vertical grid spacing smaller than 625 m is necessary to resolve properly the radiative cooling  
327 at the top of the cirrus canopy, and that the results can be quite sensitive to the radiation scheme  
328 used.

329 Meanwhile below the tropopause, time-mean radiative warming spread from 30- to 160-km  
330 radius within the cirrus canopy. The existence of radiative cooling overlying radiative warming in  
331 this region led to radiatively-forced destabilization at and below the tropopause, as was observed  
332 in Fig. 7d. Beneath the warming layer existed a region of forcing for stabilization, while a much  
333 stronger region of forcing for stabilization existed in the lower stratosphere, above the cooling  
334 maximum.



335 The results herein suggest that radiative heating tendencies played an important role in destabi-  
336 lizing the upper troposphere and stabilizing the lower stratosphere after the cirrus canopy devel-  
337 oped.

### 338 *c. The role of turbulent mixing*

339 Although vertical turbulence always acts to eliminate vertical gradients of  $\theta$ , this adjustment  
340 toward a neutral state only occurs where the mixing takes place. If turbulence occurs in a stably-  
341 stratified layer, it will act to decrease  $\theta$  at the top of the layer and increase it below. Just above and  
342 just below the mixed layer, however, the  $\theta$  profile remains undisturbed. Consequently, although  
343 turbulent mixing acts to decrease  $\partial\theta/\partial z$  in the layer in which it is occurring, it actually increases  
344  $\partial\theta/\partial z$  just below and just above the layer. These vertical gradients of turbulent mixing are quite  
345 important, particularly on the flanks of the upper-tropospheric outflow jet.

346 Two distinct maxima of vertical eddy diffusivity developed in the tropopause layer as the storm  
347 intensified (Fig. 10). Comparison of these turbulent regions to the  $N^2$  tendencies in Figs. 6c and  
348 7c reveals that the layers in which vertical eddy diffusivity maximized corresponded to layers of  
349 destabilization due to vertical turbulence. Just outside of these layers, however, vertical turbulence  
350 acted to increase  $N^2$ . The large vertical gradient of vertical eddy diffusivity near the tropopause  
351 played an important role in developing the lower-stratospheric stable layer during RI. This supports  
352 the hypothesized role of turbulence in setting the outflow-layer  $\theta$  stratification in Rotunno and  
353 Emanuel (1987).

## 354 **6. Conclusions**

355 The simulated  $N^2$  evolution shown herein closely matched that observed during the RI of Hur-  
356 ricane Patricia (2015). Three processes dominated the  $N^2$  variability in the upper troposphere and

357 lower stratosphere: advection, radiation, and vertical turbulence. Radiation and vertical turbulence  
358 played particularly important roles in developing the strong  $N^2$  maximum just above the cold-point  
359 tropopause during RI. Since these two processes are parameterized, and radiation closely depends  
360 on yet another parameterized process (microphysics), the tropopause-layer  $N^2$  variability could be  
361 quite sensitive to the assumptions inherent to the parameterizations used. A better understanding  
362 of the microphysical characteristics of the TC cirrus canopy, its interaction with radiation, and  
363 outflow-layer turbulence is critical to understanding the tropopause-layer  $N^2$  evolution.

364 In this paper, all of the variables were averaged over a full diurnal cycle to eliminate the effects  
365 of diurnal variability and isolate the overall storm evolution. Diurnal variations in static stability  
366 near the tropopause are potentially of interest with respect to the tropical cyclone diurnal cycle,  
367 however, and will be the subject of future work.

368 *Acknowledgments.* We are indebted to George Bryan for his continued development and support  
369 of Cloud Model 1. We also thank Jeffrey Kepert, Robert Fovell, and Erika Navarro for helpful  
370 conversations related to this work. This research was supported by NSF Grant #1636799.

## 371 APPENDIX

### 372 Sensitivity experiments

373 The simulations exhibited some sensitivity to the initial thermodynamic profile and the pre-  
374 scribed vertical mixing length. Although the details of the intensification and the tropopause-layer  
375  $N^2$  evolution varied when these quantities were changed, the conclusions of the paper remain  
376 unchanged.

377 *a. Sensitivity to the initial thermodynamic profile*

378 A number of sensitivity experiments were conducted using a variety of initial soundings. Chang-  
379 ing the initial temperature and humidity profiles affected the timing of the onset of organized deep  
380 convection and the rapidity of intensification. In all simulations, however, convection eventually  
381 penetrated to the tropopause, at which time vertical turbulence and radiation combined with ad-  
382 vection to adjust the  $N^2$  profile toward that which was observed in the control run. By the end of  
383 the RI period in every simulation, all three processes were actively modifying the  $N^2$  profile near  
384 the tropopause.

385 As an example, 24-hour averages of  $N^2$  are plotted in Fig. A1 for a simulation that was identical  
386 to that used in this paper, except the initial sounding was determined by averaging every CFSR  
387 grid point within 1000 km of TC Patricia's storm center at 18 UTC 21 October 2015 instead of  
388 averaging only within the 100-km radius. Although the lower-stratospheric stable layer developed  
389 more slowly and was weaker than that shown in Fig. 4, the overall evolution was quite similar and  
390 the same budget terms dominated the  $N^2$  evolution.

391 *b. Sensitivity to the vertical mixing length*

392 The rate of turbulent mixing in the Smagorinsky scheme used herein is highly dependent on a  
393 prescribed length scale. The vertical mixing length used in this paper (100 m) was based on the  
394 sensitivity experiments of Bryan (2012). Prescribing a smaller mixing length produces smaller  
395  $\theta$  tendencies due to turbulence, but even with a mixing length on the low end of those tested  
396 by Bryan (2012), turbulence still played an important role in the tropopause-layer  $N^2$  evolution.  
397 Fig. A2 shows the 24-hour-averaged contributions of turbulent mixing to the  $N^2$  evolution from  
398 a simulation identical to that used in this paper, except with a vertical mixing length of 50 m. At

all times, vertical turbulence still played an important role in the tropopause-layer  $N^2$  evolution,  
particularly during the latter stages of RI (48-72 hours).

## References

- Bryan, G. H., 2012: Effects of surface exchange coefficients and turbulence length scales on the intensity and structure of numerically simulated hurricanes. *Mon. Wea. Rev.*, **140**, 1125–1143.
- Bryan, G. H., cited 2018: The governing equations for CM1. [Available online at [http://www2.mmm.ucar.edu/people/bryan/cm1/cm1\\_equations.pdf](http://www2.mmm.ucar.edu/people/bryan/cm1/cm1_equations.pdf)].
- Bryan, G. H., and R. Rotunno, 2009: The maximum intensity of tropical cyclones in axisymmetric numerical model simulations. *Mon. Wea. Rev.*, **137**, 1770–1789.
- Bu, Y. P., R. G. Fovell, and K. L. Corbosiero, 2014: Influence of cloud-radiative forcing on tropical cyclone structure. *J. Atmos. Sci.*, **71**, 1644–1622.
- Doyle, J. D., and Coauthors, 2017: A view of tropical cyclones from above: The Tropical Cyclone Intensity (TCI) Experiment. *Bull. Amer. Meteor. Soc.*, **98**, 2113–2134.
- Duran, P., and J. Molinari, 2018: Dramatic inner-core tropopause variability during the rapid intensification of Hurricane Patricia (2015). *Mon. Wea. Rev.*, **146**, 119–134.
- Emanuel, K., 2012: Self-stratification of tropical cyclone outflow. Part II: Implications for storm intensification. *J. Atmos. Sci.*, **69**, 988–996.
- Emanuel, K., and R. Rotunno, 2011: Self-stratification of tropical cyclone outflow. Part I: Implications for storm structure. *J. Atmos. Sci.*, **68**, 2236–2249.

418 Iacono, M. J., J. S. Delamere, E. J. Mlawer, M. W. Shephard, S. A. Clough, and W. D. Collins,  
 419 2008: Radiative forcing by long-lived greenhouse gases: Calculations with the AER radiative  
 420 transfer models. *J. Geophys. Res.*, **113** (D13103).

421 Kepert, J. D., J. Schwendike, and H. Ramsay, 2016: Why is the tropical cyclone boundary layer  
 422 not "well mixed"? *J. Atmos. Sci.*, **73**, 957–973.

423 Kieu, C., V. Tallapragada, D.-L. Zhang, and Z. Moon, 2016: On the development of double warm-  
 424 core structures in intense tropical cyclones. *J. Atmos. Sci.*, **73**, 4487–4506.

425 Kimberlain, T. B., E. S. Blake, and J. P. Cangialosi, 2016: Tropical cyclone report: Hurricane  
 426 Patricia. National Hurricane Center. [Available online at [www.nhc.noaa.gov](http://www.nhc.noaa.gov)].

427 Komaromi, W. A., and J. D. Doyle, 2017: Tropical cyclone outflow and warm core structure as  
 428 revealed by HS3 dropsonde data. *Mon. Wea. Rev.*, **145**, 1339–1359.

429 Markowski, P. M., and G. H. Bryan, 2016: LES of laminar flow in the PBL: A potential problem  
 430 for convective storm simulations. *Mon. Wea. Rev.*, **144**, 1841–1850.

431 Ohno, T., and M. Satoh, 2015: On the warm core of a tropical cyclone formed near the tropopause.  
 432 *J. Atmos. Sci.*, **72**, 551–571.

433 Rogers, R. F., S. Aberson, M. M. Bell, D. J. Cecil, J. D. Doyle, J. Morgerman, L. K. Shay, and  
 434 C. Velden, 2017: Re-writing the tropical record books: The extraordinary intensification of  
 435 Hurricane Patricia (2015). *Bull. Amer. Meteor. Soc.*, **98**, 2091–2112.

436 Rotunno, R., and K. A. Emanuel, 1987: An air-sea interaction theory for tropical cyclones. Part II:  
 437 Evolutionary study using a nonhydrostatic axisymmetric numerical model. *J. Atmos. Sci.*, **44**,  
 438 542–561.

439 Stern, D. P., and F. Zhang, 2013: How does the eye warm? Part I: A potential temperature budget  
440 analysis of an idealized tropical cyclone. *J. Atmos. Sci.*, **70**, 73–89.

441 Thompson, G., R. M. Rasmussen, and K. Manning, 2004: Explicit forecasts of winter precipitation  
442 using an improved bulk microphysics scheme. Part I: Description and sensitivity analysis. *Mon.*  
443 *Wea. Rev.*, **132**, 519–542.

444 Trier, S. B., and R. D. Sharman, 2009: Convection-permitting simulations of the environment sup-  
445 porting widespread turbulence within the upper-level outflow of a mesoscale convective system.  
446 *Mon. Wea. Rev.*, **137**, 1972–1990.

## 447 LIST OF FIGURES

- 448 **Fig. 1.** The maximum 10-m wind speed (top panel;  $\text{m s}^{-1}$ ) and minimum sea-level pressure (bottom  
449 panel; hPa) in the simulated storm (blue lines; plotted every minute) and from Hurricane  
450 Patricia's best track (red stars; plotted every six hours beginning at the time Patricia attained  
451 tropical storm intensity). The rapid weakening during the later stage of Patricia's lifetime  
452 was induced by landfall. . . . . 26
- 453 **Fig. 2.** Left panels: Twenty-four-hour changes in squared Brunt-Väisälä frequency ( $N^2$ ;  $10^{-4} \text{ s}^{-2}$ )  
454 computed using Eq. 8 over (top row) 0-24 hours, (middle row) 24-48 hours, (bottom row)  
455 48-72 hours. Middle Panels: The  $N^2$  change over the same time periods computed using Eqs.  
456 4-7, Right Panels: The budget residual over the same time periods, computed by subtracting  
457 the budget change (middle column) from the model change (left column). Orange lines  
458 represent the cold-point tropopause height averaged over the same time periods. . . . . 27
- 459 **Fig. 3.** Time series of the contribution of each of the budget terms to the time tendency of the  
460 squared Brunt-Väisälä frequency ( $N^2$ ;  $10^{-4} \text{ s}^{-2}$ ). For each budget term, the absolute value  
461 of the  $N^2$  tendency is averaged temporally over 1-hour periods (using output every minute),  
462 and spatially in a region extending from 0 to 200 km radius and 14 to 21 km altitude. . . . . 28
- 463 **Fig. 4.** Twenty-four-hour averages of squared Brunt-Väisälä frequency ( $N^2$ ;  $10^{-4} \text{ s}^{-2}$ ) over (a) 0-24  
464 hours, (b) 24-48 hours, (c) 48-72 hours. Orange lines represent the cold-point tropopause  
465 height averaged over the same time periods. . . . . 29
- 466 **Fig. 5.** (a) Total change in  $N^2$  over the 0-24-hour period ( $10^{-4} \text{ s}^{-2} (24 \text{ h})^{-1}$ ) and the contributions to  
467 that change from (b) the sum of horizontal and vertical advection, (c) vertical turbulence, (d)  
468 longwave and shortwave radiation, (e) the sum of horizontal advection, vertical advection,

469	and vertical turbulence, and (f) the sum of horizontal advection, vertical advection, vertical	
470	turbulence, and longwave and shortwave radiation. Orange lines represent the cold-point	
471	tropopause height averaged over the 0-24-hour period. . . . .	31
472	<b>Fig. 6.</b> As in Fig. 5, but for the 24-48-hour period. . . . .	32
473	<b>Fig. 7.</b> As in Fig. 5, but for the 48-72-hour period. . . . .	33
474	<b>Fig. 8.</b> The contributions to the change in $N^2$ over the 24-48-hour period ( $10^{-4} \text{ s}^{-2} (24 \text{ h})^{-1}$ ) by	
475	(a) horizontal advection and (b) vertical advection. (c) The radial velocity ( $\text{m s}^{-1}$ ; filled con-	
476	tours), potential temperature (K; thick black contours), cold-point tropopause height (orange	
477	line), and level of maximum outflow (dashed cyan line) averaged over the 24-48-hour period.	
478	(d) The vertical velocity ( $\text{cm s}^{-1}$ ; filled contours), potential temperature (K; thick black con-	
479	tours), and cold-point tropopause height (orange line) averaged over the 24-48-hour period.	
480	34	
481	<b>Fig. 9.</b> Ice mixing ratio ( $\text{g kg}^{-1}$ ) and cold-point tropopause height (orange lines) averaged over (a)	
482	0-24 hours, (c) 24-48 hours, and (e) 48-72 hours. Radiative heating rate ( $\text{K h}^{-1}$ ) and cold-	
483	point tropopause height (orange lines) averaged over (b) 0-24 hours, (d) 24-48 hours, and (f)	
484	48-72 hours. . . . .	36
485	<b>Fig. 10.</b> Vertical eddy diffusivity ( $\text{m}^2 \text{ s}^{-2}$ ; filled contours), cold-point tropopause height (cyan lines),	
486	and radial velocity ( $\text{m s}^{-1}$ ; thick black lines) averaged over (a) 0-24 hours, (b) 24-48 hours,	
487	and (c) 48-72 hours. . . . .	37
488	<b>Fig. A1.</b> Twenty-four-hour averages of squared Brunt-Väisälä frequency ( $N^2$ ; $10^{-4} \text{ s}^{-2}$ ) over (a) 0-24	
489	hours, (b) 24-48 hours, (c) 48-72 hours, and (d) 72-96 hours for the simulation described	



490 in Appendix Aa. Orange lines represent the cold-point tropopause height averaged over the  
 491 same time periods. . . . . 38

492 **Fig. A2.** The contribution of vertical turbulence to the  $N^2$  variability ( $10^{-4} \text{ s}^{-2} (24 \text{ h})^{-1}$ ) averaged  
 493 over (a) 0-24 hours, (b) 24-48 hours, (c) 48-72 hours, and (d) 72-96 hours for the simulation  
 494 described in Appendix Ab. Orange lines represent the cold-point tropopause height averaged  
 495 over the same time periods. . . . . 39

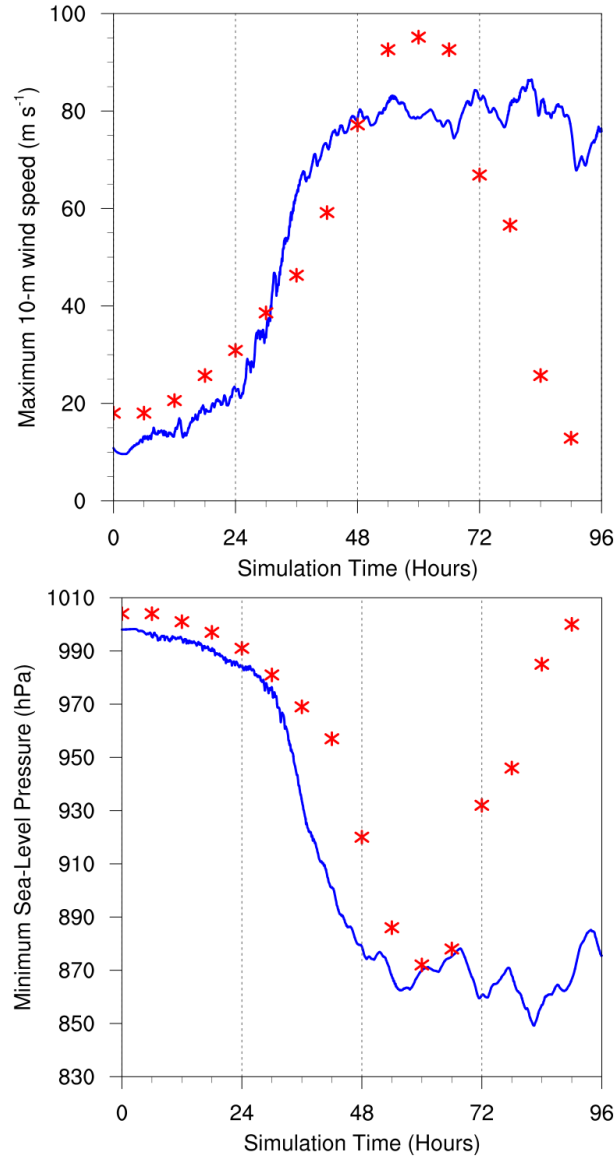


FIG. 1. The maximum 10-m wind speed (top panel;  $\text{m s}^{-1}$ ) and minimum sea-level pressure (bottom panel; hPa) in the simulated storm (blue lines; plotted every minute) and from Hurricane Patricia's best track (red stars; plotted every six hours beginning at the time Patricia attained tropical storm intensity). The rapid weakening during the later stage of Patricia's lifetime was induced by landfall.

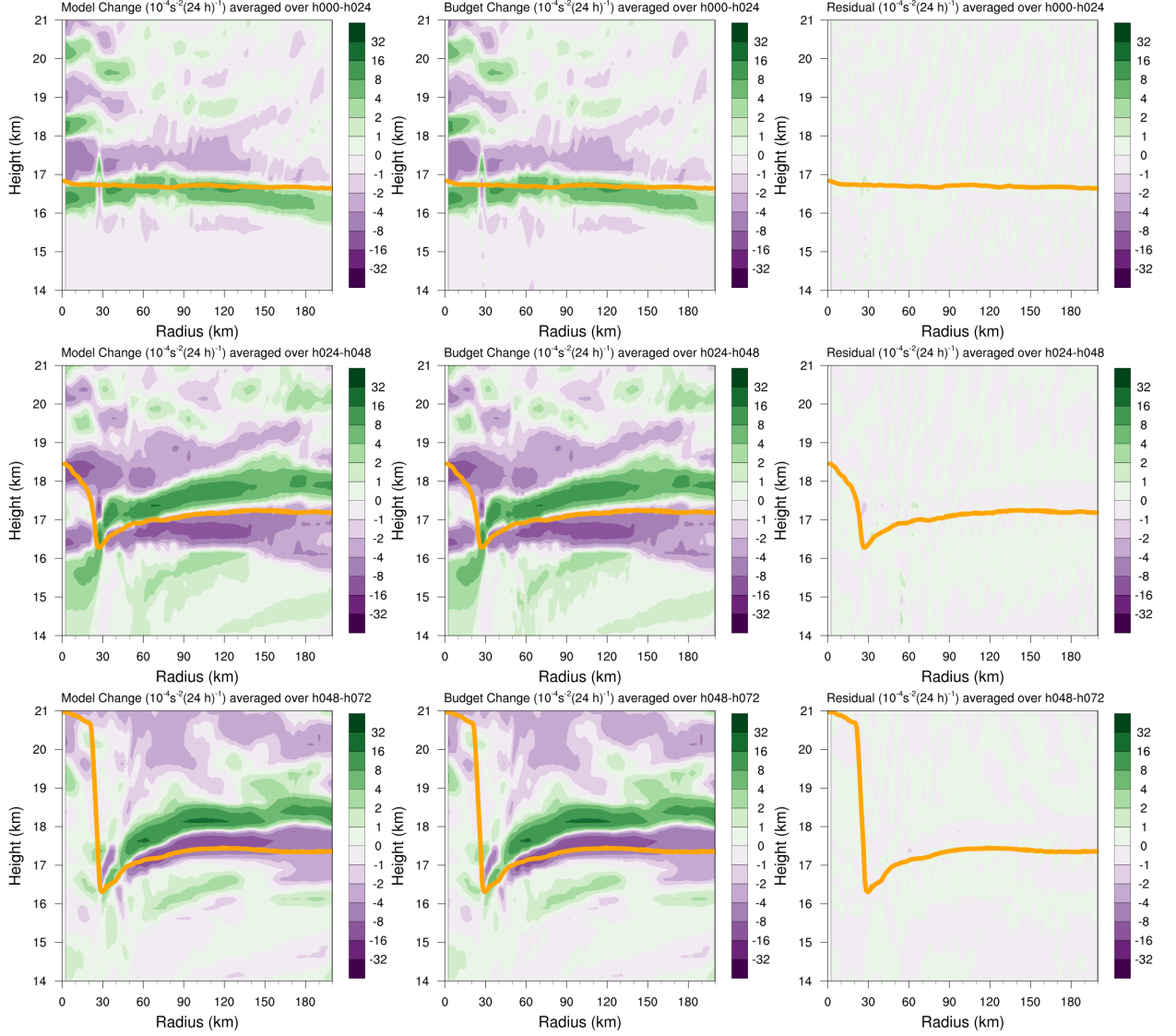


FIG. 2. Left panels: Twenty-four-hour changes in squared Brunt-Väisälä frequency ( $N^2$ ;  $10^{-4} \text{ s}^{-2}$ ) computed using Eq. 8 over (top row) 0-24 hours, (middle row) 24-48 hours, (bottom row) 48-72 hours. Middle Panels: The  $N^2$  change over the same time periods computed using Eqs. 4-7, Right Panels: The budget residual over the same time periods, computed by subtracting the budget change (middle column) from the model change (left column). Orange lines represent the cold-point tropopause height averaged over the same time periods.

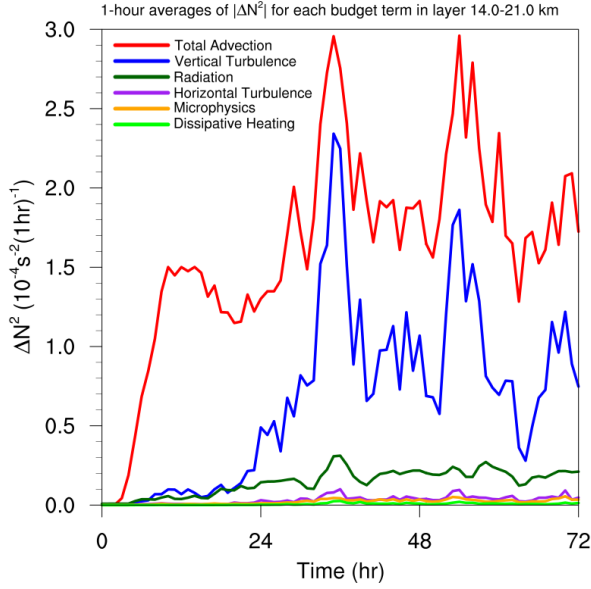
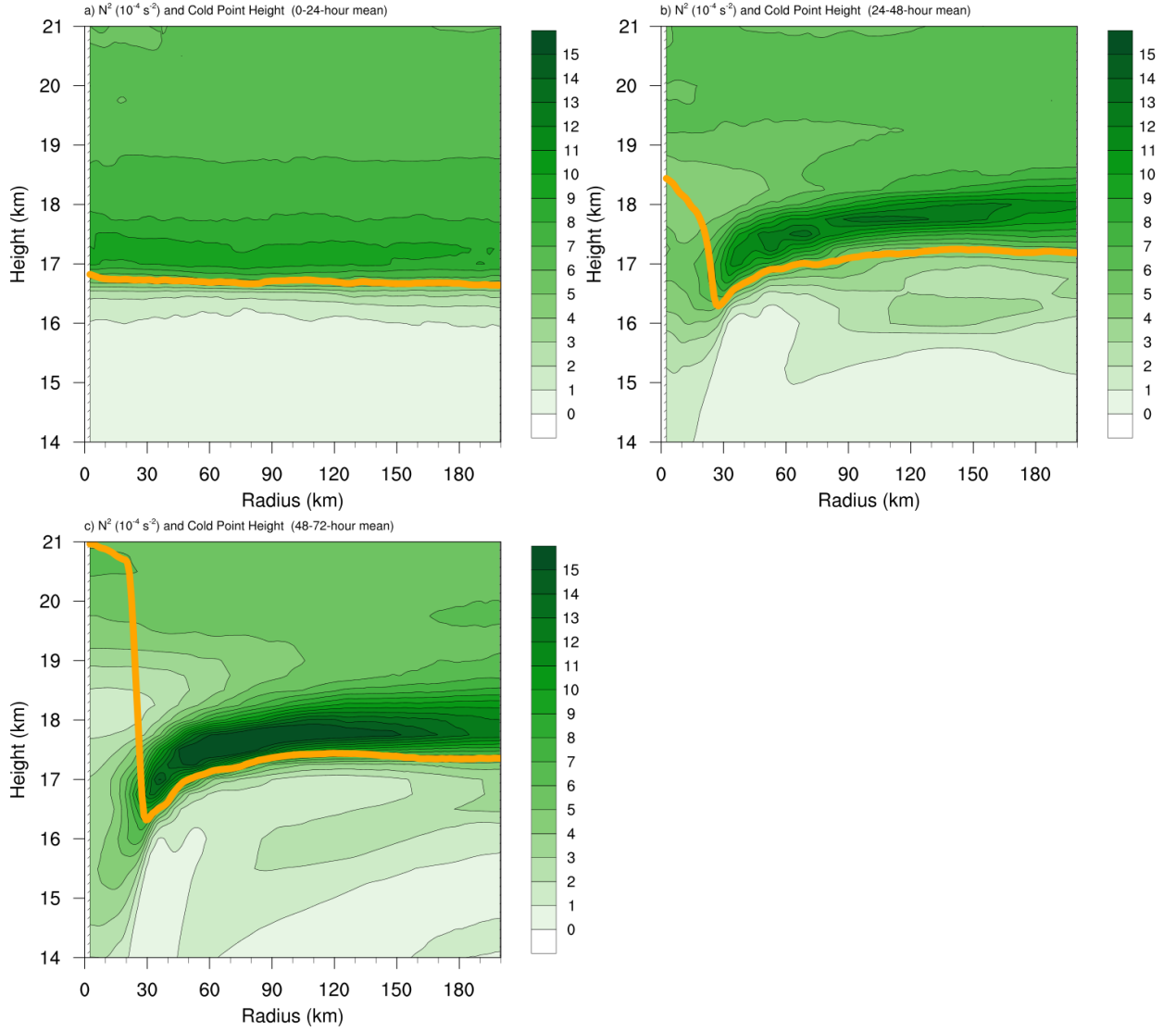
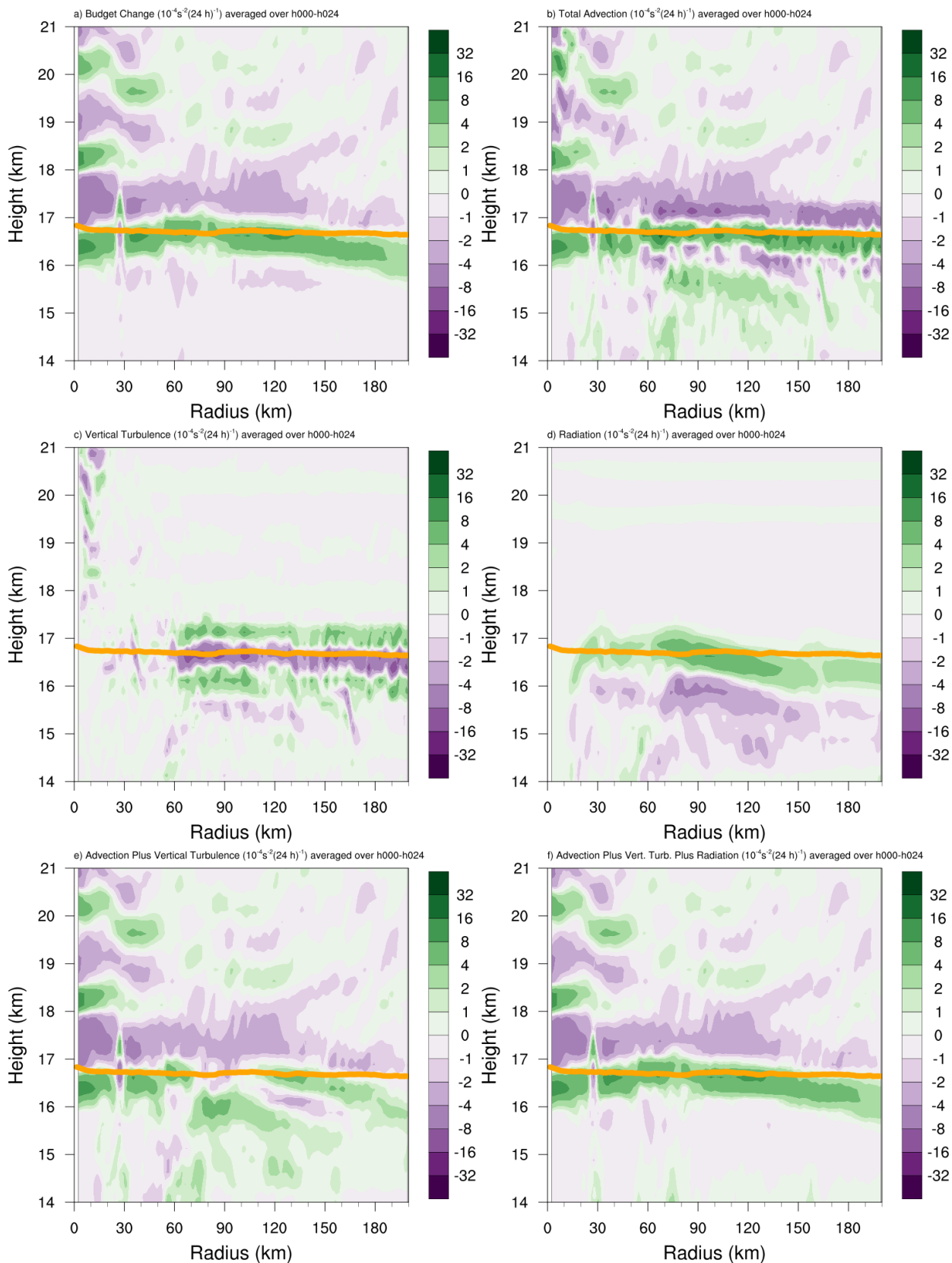


FIG. 3. Time series of the contribution of each of the budget terms to the time tendency of the squared Brunt-Väisälä frequency ( $N^2$ ;  $10^{-4} \text{ s}^{-2}$ ). For each budget term, the absolute value of the  $N^2$  tendency is averaged temporally over 1-hour periods (using output every minute), and spatially in a region extending from 0 to 200 km radius and 14 to 21 km altitude.



509 FIG. 4. Twenty-four-hour averages of squared Brunt-Väisälä frequency ( $N^2$ ;  $10^{-4} \text{ s}^{-2}$ ) over (a) 0-24 hours, (b)  
 510 24-48 hours, (c) 48-72 hours. Orange lines represent the cold-point tropopause height averaged over the same  
 511 time periods.



512 FIG. 5. (a) Total change in  $N^2$  over the 0-24-hour period ( $10^{-4} \text{ s}^{-2} (24 \text{ h})^{-1}$ ) and the contributions to that change  
513 from (b) the sum of horizontal and vertical advection, (c) vertical turbulence, (d) longwave and shortwave  
514 radiation, (e) the sum of horizontal advection, vertical advection, and vertical turbulence, and (f) the sum of  
515 horizontal advection, vertical advection, vertical turbulence, and longwave and shortwave radiation. Orange  
516 lines represent the cold-point tropopause height averaged over the 0-24-hour period.

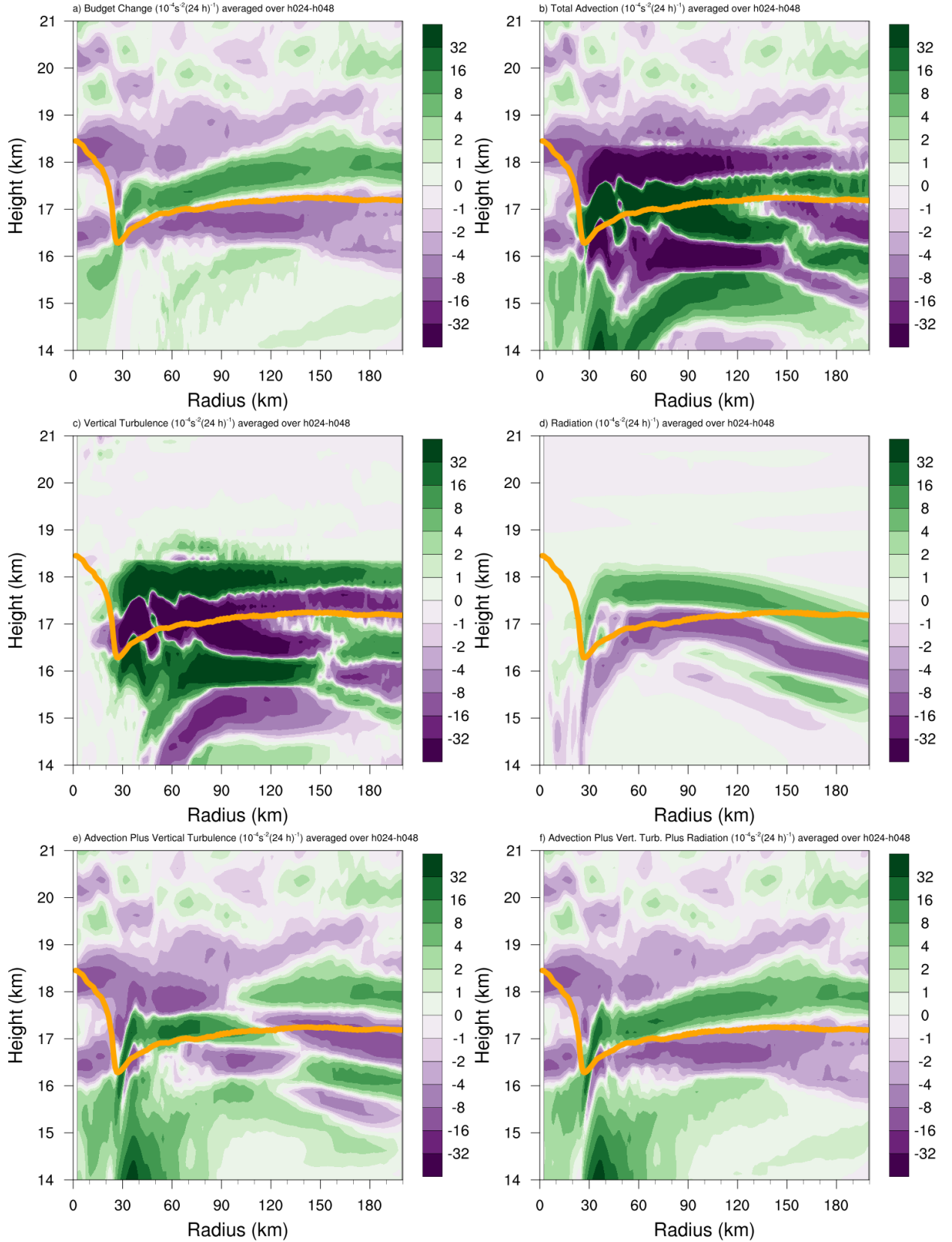


FIG. 6. As in Fig. 5, but for the 24-48-hour period.



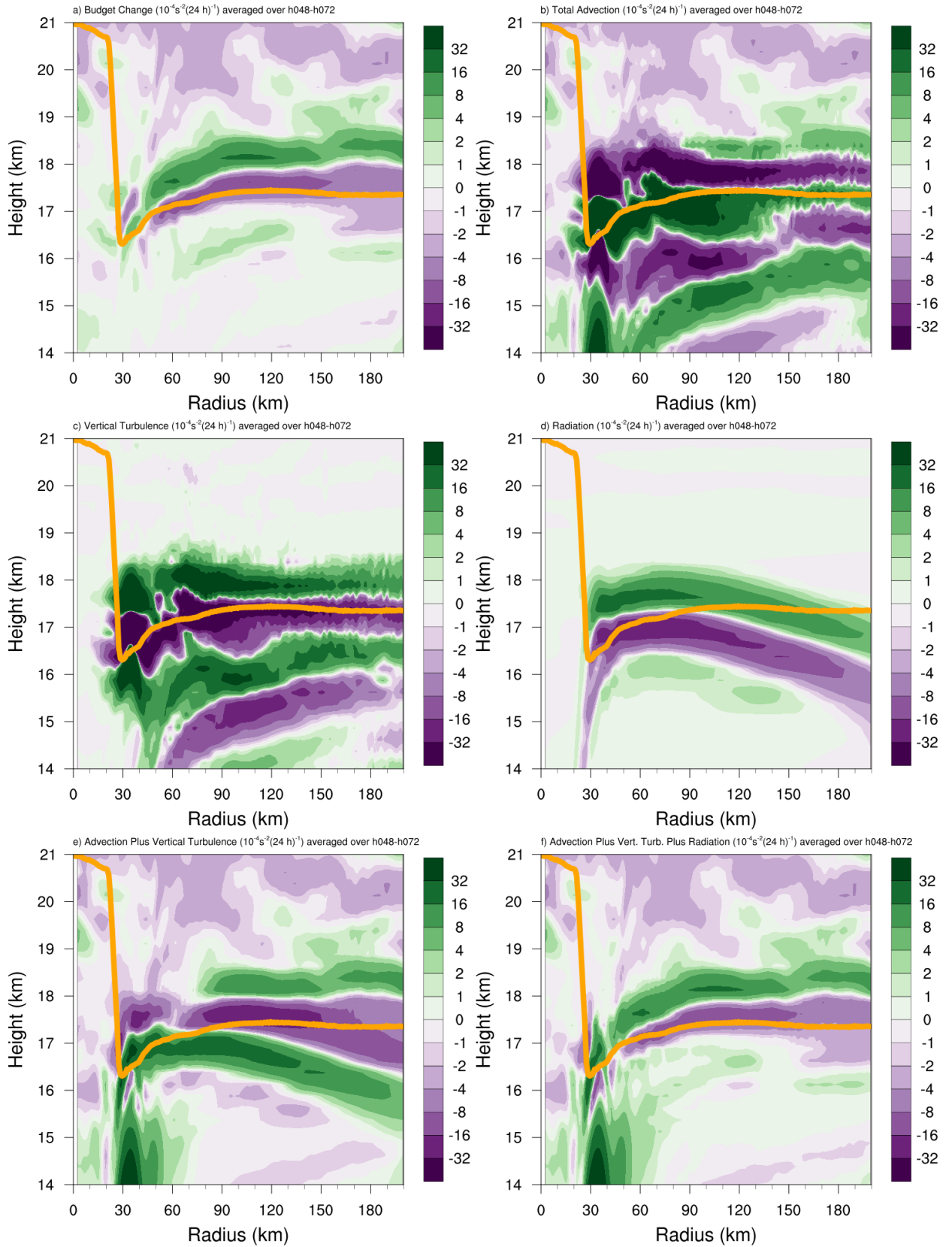


FIG. 7. As in Fig. 5, but for the 48-72-hour period.

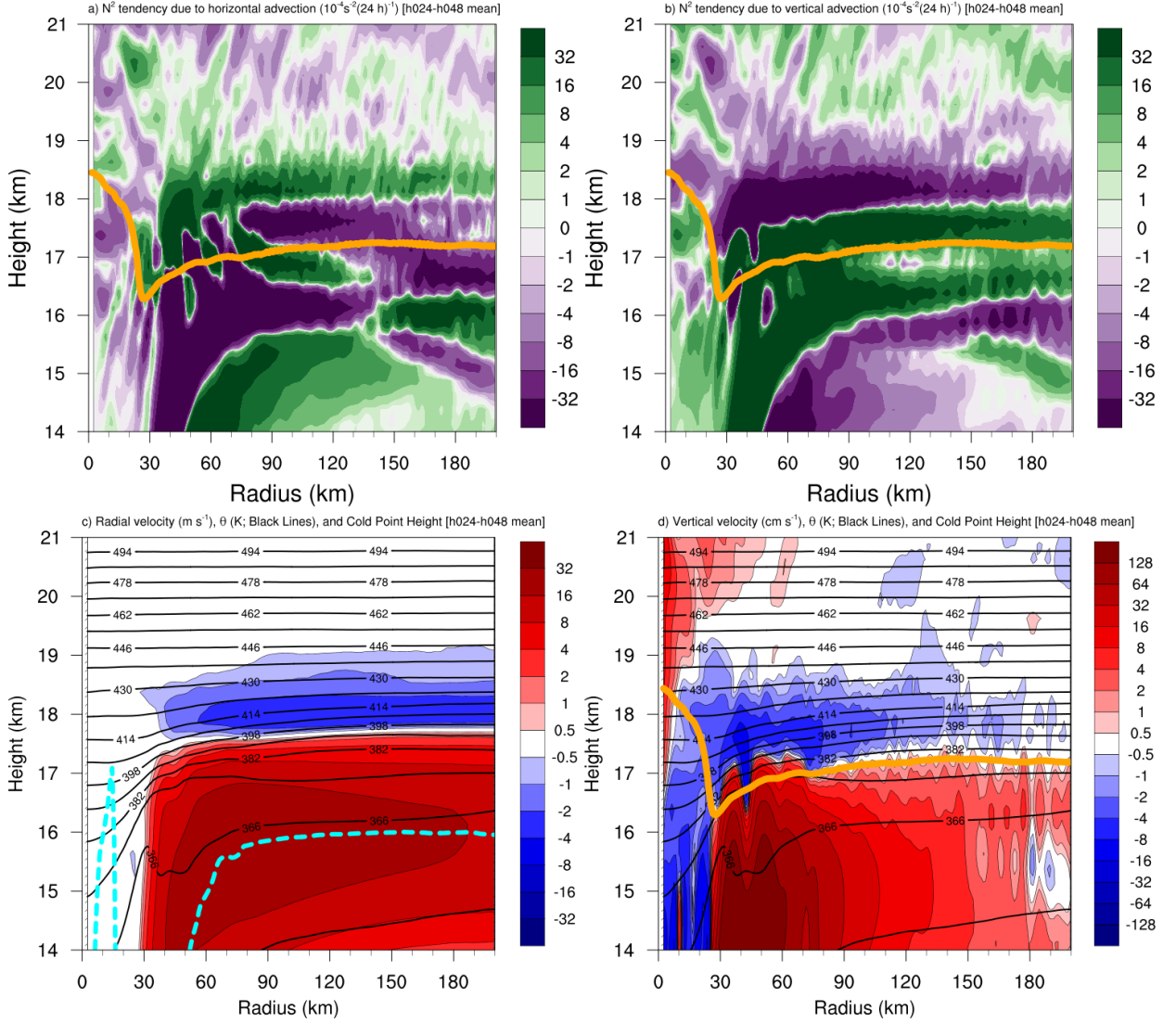
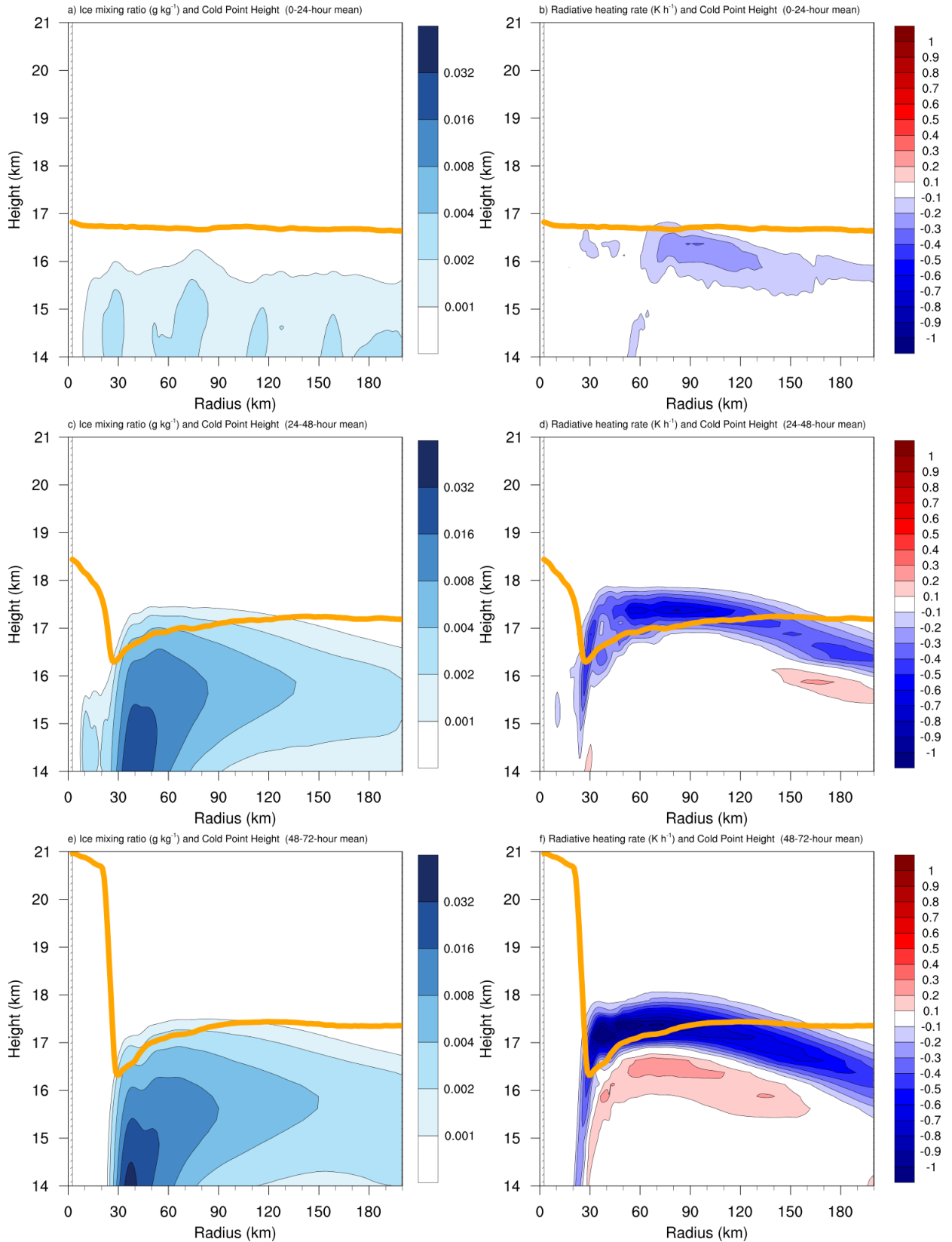


FIG. 8. The contributions to the change in  $N^2$  over the 24-48-hour period ( $10^{-4} \text{ s}^{-2} (24 \text{ h})^{-1}$ ) by (a) horizontal advection and (b) vertical advection. (c) The radial velocity ( $\text{m s}^{-1}$ ; filled contours), potential temperature (K; thick black contours), cold-point tropopause height (orange line), and level of maximum outflow (dashed cyan line) averaged over the 24-48-hour period. (d) The vertical velocity ( $\text{cm s}^{-1}$ ; filled contours), potential temperature (K; thick black contours), and cold-point tropopause height (orange line) averaged over the 24-48-hour period.



523 FIG. 9. Ice mixing ratio ( $\text{g kg}^{-1}$ ) and cold-point tropopause height (orange lines) averaged over (a) 0-24 hours,  
524 (c) 24-48 hours, and (e) 48-72 hours. Radiative heating rate ( $\text{K h}^{-1}$ ) and cold-point tropopause height (orange  
525 lines) averaged over (b) 0-24 hours, (d) 24-48 hours, and (f) 48-72 hours.

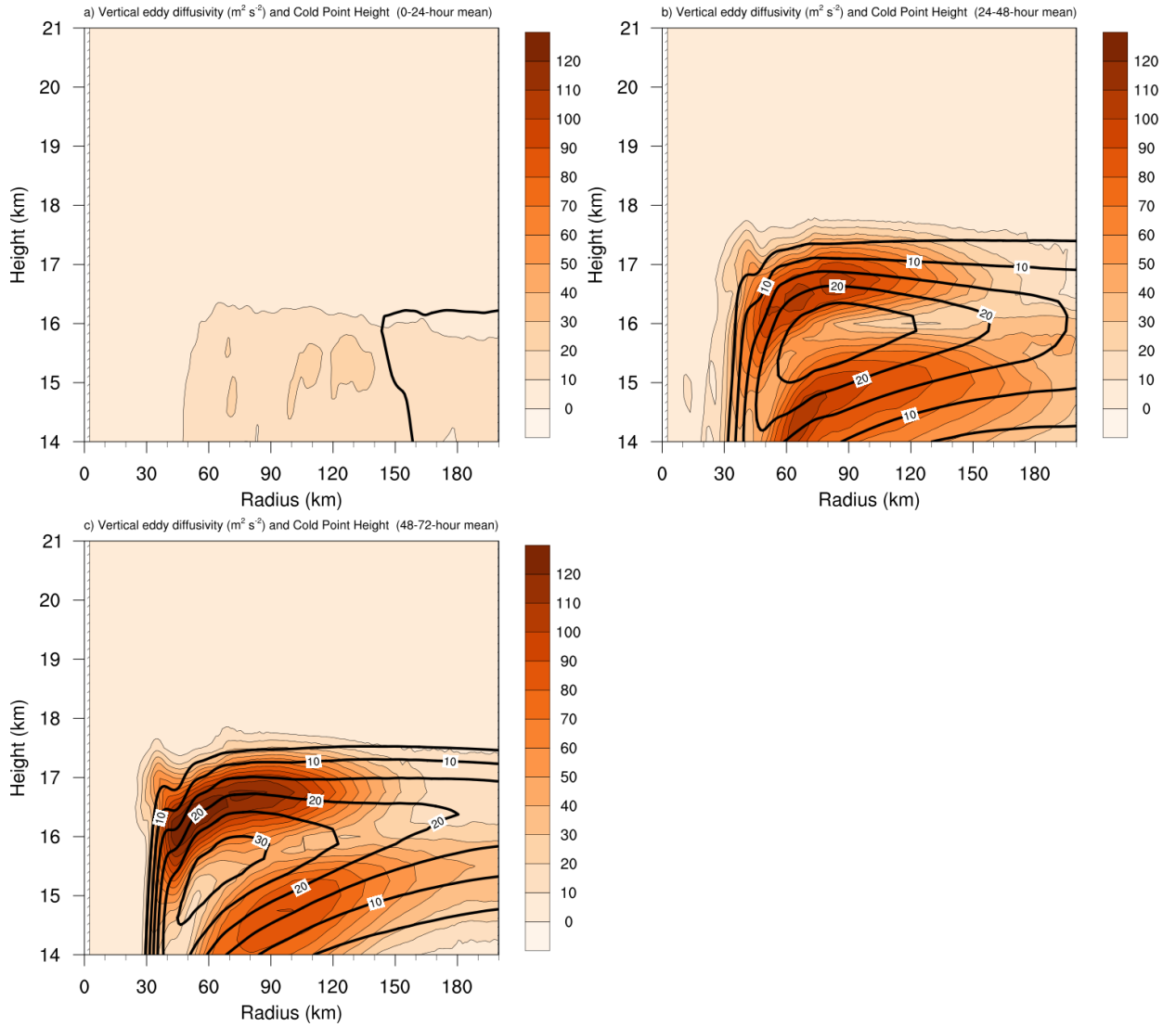
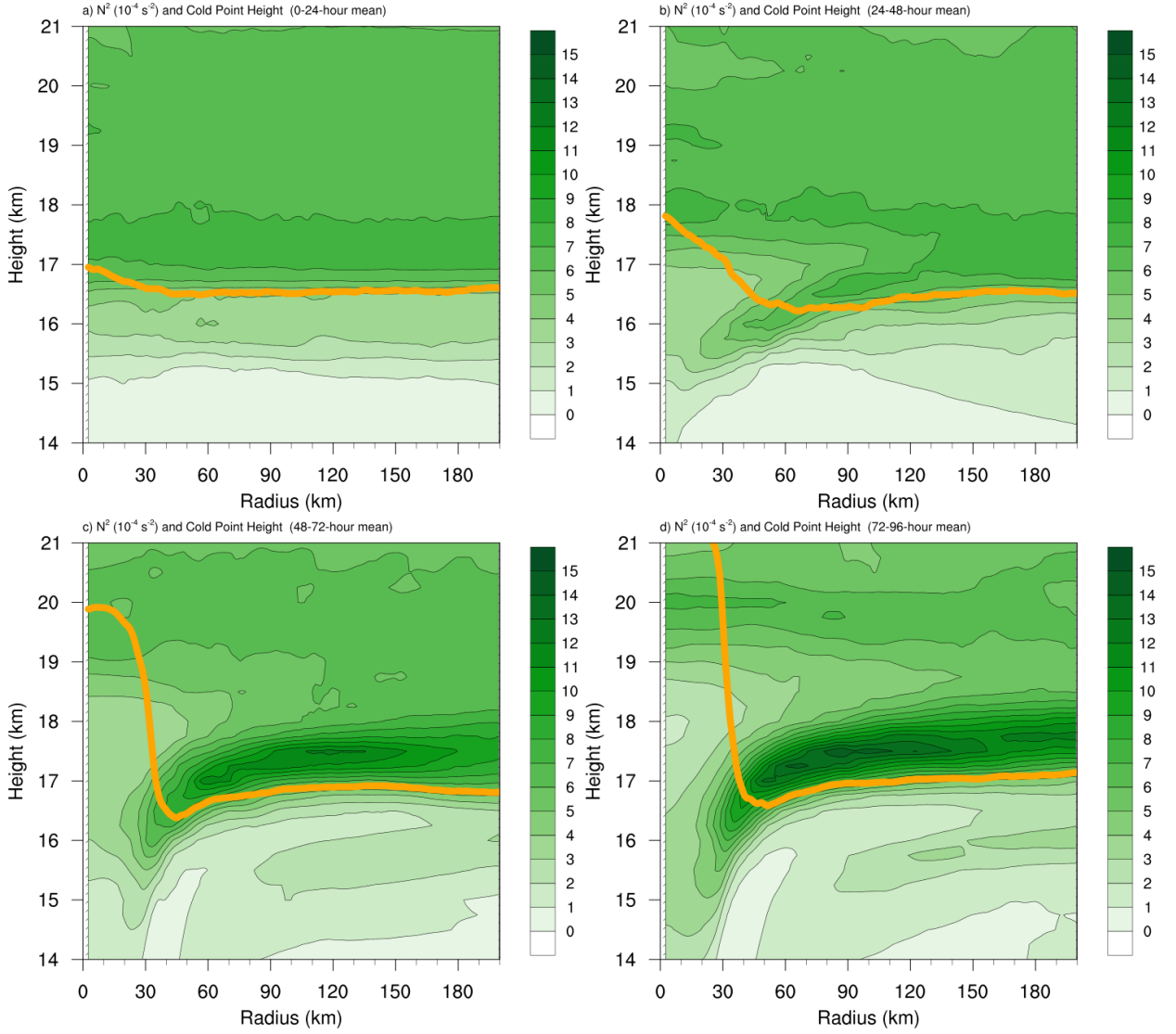


FIG. 10. Vertical eddy diffusivity ( $\text{m}^2 \text{s}^{-2}$ ; filled contours), cold-point tropopause height (cyan lines), and radial velocity ( $\text{m s}^{-1}$ ; thick black lines) averaged over (a) 0-24 hours, (b) 24-48 hours, and (c) 48-72 hours.



528 Fig. A1. Twenty-four-hour averages of squared Brunt-Väisälä frequency ( $N^2$ ;  $10^{-4} \text{ s}^{-2}$ ) over (a) 0-24 hours,  
 529 (b) 24-48 hours, (c) 48-72 hours, and (d) 72-96 hours for the simulation described in Appendix Aa. Orange lines  
 530 represent the cold-point tropopause height averaged over the same time periods.

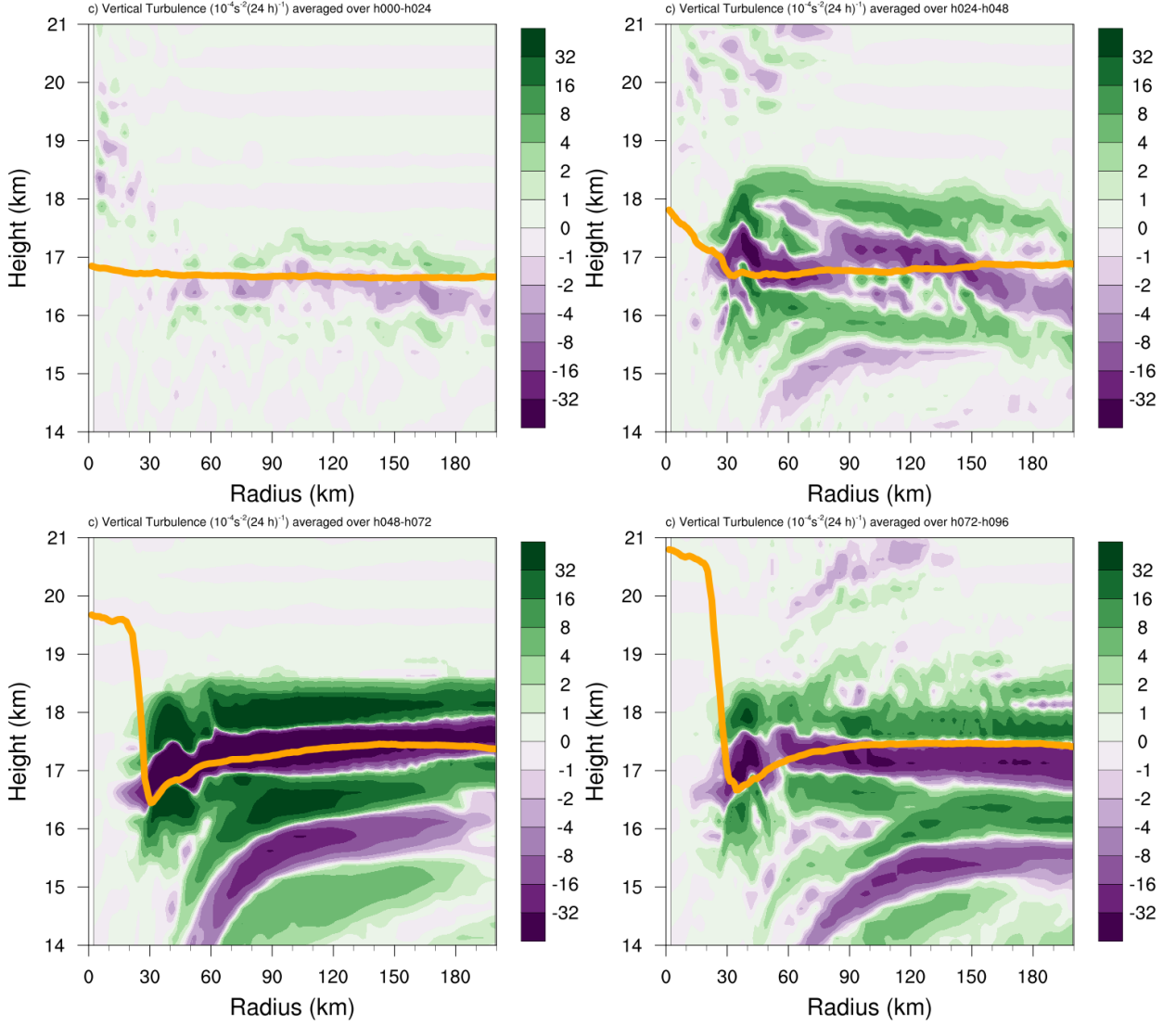


Fig. A2. The contribution of vertical turbulence to the  $N^2$  variability ( $10^{-4} \text{ s}^{-2} (24 \text{ h})^{-1}$ ) averaged over (a) 0-24 hours, (b) 24-48 hours, (c) 48-72 hours, and (d) 72-96 hours for the simulation described in Appendix Ab. Orange lines represent the cold-point tropopause height averaged over the same time periods.